Interface thermal behavior in nanomaterials by thermal grating relaxation

Pier Luca Palla, Sonia Zampa, Évelyne Martin, Fabrizio Cleri

Interface thermal behavior in nanomaterials by thermal grating relaxation

Pier Luca Palla*, Sonia Zampa, Evelyne Lampin, Fabrizio Cleri

[a]*Institut d'Electronique, Microelectronique et Nanotechnologie (IEMN, UMR CNRS 8520),Université de Lille I, 59652 Villeneuve d'Ascq, France*

Abstract

We study the relaxation of a thermal grating in multilayer materials with interface thermal resistances. The analytical development allows for the numerical determination of this thermal property in Approach to Equilibrium Molecular Dynamics and suggests an experimental setup for its measurement. Possible non-diffusive effects at the nanoscale are take into consideration by a non-local formulation of the heat equation. As a case study, we numerically apply the present approach to silicon grain boundary thermal resistance.

Keywords: Interface thermal resistance, Laser Induced Thermal Grating, Non-local heat transfer, Scale effects, Approach to Equilibrium Molecular Dynamics, Grain boundary

1. Introduction

In this work, we address the heat transport in heterogeneous nanostructured systems. At small scale, where the surface to volume ratio increases, the behavior of the interfaces between homogeneous regions is no longer neg-

*Corresponding author
Email address: pier-luca.palla@isen.iemn.univ-lille1.fr (Pier Luca Palla)

ligible. Moreover, at least for materials with a large phonon mean free path, also the thermal conductivity of the bulk can deviate from the macroscopic picture, i.e. scale effects can arise. On the other hand, in numerical as in experimental studies, it is often difficult to distinguish between the bulk and the interfaces role in the thermal response of the overall system. In order to investigate these issues, we consider here a particular thermal processing, namely the relaxation of a spatially periodic temperature profile, in heterogeneous structures. This thermal processing is exploited as well as in numerical techniques, as the Approach to Equilibrium Molecular Dynamics (AEMD) [1], in experimental approaches, as Laser-Induced Thermal Grating (LITG) [2], and in theoretical works [3]. The underlying idea is to generate a periodic temperature profile or thermal grating (TG) in the system (see Fig. 1) and to observe its equilibration time. This in turn can be related to the thermal or thermoelastic properties of the media. Generally speaking, both coherent sound waves and incoherent thermal excitations are induced in the sample [4]. Nevertheless, the most of the energy is stored in the temperature grating [5, 6]. Therefore, the relaxation is usually described by thermal transport models. In particular, by considering a classical diffusive thermal transport, the heat equation predicts an exponential decay of the amplitude of the TG with a characteristic time τ related to the thermal conductivity k according to

$$k = \frac{cL^2}{4\pi^2\tau} \tag{1}$$

where L is the spatial period of the TG and c the volumetric heat capacity of the bulk material.

To obtain the temperature profile in LITG experiments, two short laser

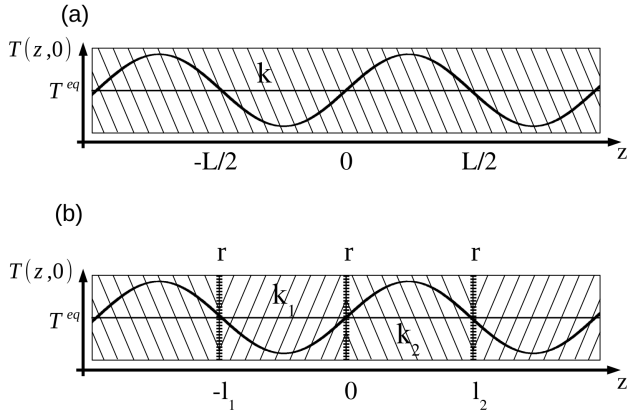

Figure 1: Schematic representation of a periodic temperature profile (thermal grating) in a bulk material of thermal conductivity k (top panel) and in bilayer system, of periodicity $L = l_1 + l_2$, composed by two materials of conductivity k_1 and k_2 joined by interfaces of thermal resistance r (bottom panel).

pulses of central wavelength λ are crossed on a sample resulting in an interference pattern with period $L = \lambda/2\sin(\theta/2)$ defined by the angle θ between the beams. Absorption of laser light leads to a sinusoidal temperature profile, and the temporal decay of this TG is monitored via diffraction of a probe laser beam so to measure the bulk conductivity of the medium. LITG spectroscopy has been widely used in thermal characterizations of materials [2] including, e.g., silicon membranes [2, 7], and in gas phase diagnostics [8].

A similar protocol is implemented in AEMD atomistic simulations. This numerical technique has been developed in the context of molecular dynamics with the aim of studying the thermal transport in dielectric materials [1]. It provides a very efficient and robust method to investigate thermal properties in a wide range of system sizes. AEMD has been applied by several authors to the calculation of the thermal conductivity in c-Si,c-Ge and α-quartz [1],

in Si/Ge nanocomposite [9], in Si nanowires [10] and in graphene-based structures [11, 12]. Initially developed for classical Molecular Dynamics (MD) this technique has been recently implemented in ab-initio calculations as well [13].

These applications of the thermal grating relaxation address the study of the thermal conductivity in bulk materials. In this paper, with the aim of extending the AEMD method and of proposing a new experimental setup for thermal studies, we consider a more general configuration. We address heat conduction in bilayer systems composed of two homogeneous materials (see Fig. 1-b), joined through non-ideal interfaces [14]. In particular, a resistive interfacial thermal effect is modeled using a Kapitza resistance [15]. From the mathematical point of view, this problem represents a further generalization of the *Sommerfeld heat-conduction problem for a ring* [16], successively extended by I.R. Vengerov to the case of two different media simply connected via an ideal interface [17]. As we will show in the following, the present development allows for the theoretical prediction of the ITR in the context of the AEMD. Moreover, the results suggest that this approach can be adopted in LITG as well. Therefore, it could provide a direct access to the experimental determination of the interface thermal resistance (ITR).

This thermal property, usually negligible in macroscopic structures, is attracting by contrast increasing attention in nanotechnology. For instance, the removal of the heat generated by electronic systems, one of the crucial constraint on the performance of modern nanoelectronics, is largely limited by interfaces between layers. In silicon based thermoelectric nanomaterials, the grains boundaries resistance allows for a significant increasing of the figure of merit.

One of the main theoretical limits in projecting down to the nanoscale the thermal grating based techniques is the validity of the Fourier's law at such a scale. We address this crucial point by considering a non-local formulation of the heat conduction problem. In other words, we introduce in the analytical model a wavelength dependence of the bulk thermal conductivity. This improvement perfectly matches the results of the corresponding numerical simulations showing that, at least down to a given scale, a non-local approach to the thermal transport allows for a correct description of the ballistic effects in nanostrucured systems.

The paper is organized as follows. For the sake of clarity, in Section 2, we firstly resume the solution of the heat equation for a periodic bulk system (heat-conduction problem for a ring) and its application in AEMD simulations [1]. Then, we generalize the mathematical problem to the bilayer case. In Section 3, we discuss the results of numerical simulations of a bilayer material, namely of a periodic system composed by slabs of crystal silicon (c-Si) with different crystallographic directions connected by grain boundaries (GB). The details of the simulations and of the GB model adopted in this work are reported in Appendix A. In Section 4, we show that the numerical results for the c-Si bulk conductivity [1] can be modeled by a non-local formulation of the heat equation. This interpretation is then applied in Section 5 to the calculation of the ITR of silicon GB. Finally, in Section 6 we discuss the application of the present developments in LITG experiments, supplying a further analysis obtained by additional numerical simulations.

2. Heat-conduction problem on a ring

2.1. Bulk system

We start by considering a mono-dimensional heat conduction problem for an homogeneous media under periodic boundary conditions (PBC). According to the classical theory, the heat transfer is governed by the heat equation:

$$c\frac{\partial T(z,t)}{\partial t} = k\frac{\partial^2 T(z,t)}{\partial z^2} \tag{2}$$

involving the classical field of temperature $T(z,t)$, and by the PBC:

$$T(0,t) = T(L,t) \tag{3}$$

$$\frac{\partial T(0,t)}{\partial z} = \frac{\partial T(L,t)}{\partial z} \tag{4}$$

Eq. (3) states the periodicity of the solution and, in particular, the continuity of the temperature field across the periodic boundaries. Eq. (4) represents the continuity of the heat flux according to the Fourier's Law

$$J(z,t) = -k\frac{\partial T(z,t)}{\partial z} \tag{5}$$

or, equivalently, the conservation of the energy.

For an arbitrary initial condition $T(z,0)$ $z \in [-\frac{L}{2}, \frac{L}{2}]$, the well-known solution of the heat equation is

$$T(z,t) = T^{eq} + \sum_{n=1}^{\infty} \left[A_n cos(\alpha_n^0 z) + B_n sin(\alpha_n^0 z)\right] e^{-\frac{t}{\tau_n^0}} \tag{6}$$

where T^{eq} is the asymptotically target temperature and

$$\tau_n^0 = \frac{c}{k(\alpha_n^0)^2} \tag{7}$$

The PBC in Eqs. (3) and (4) impose the following set of wavenumbers:

$$\alpha_n^0 = n\frac{2\pi}{L} \tag{8}$$

The coefficients A_n and B_n are the components of the Fourier series of $T(z,0)$. Eq. (6) shows that each term in the series is damped by an exponential factor with characteristic time τ_n^0. Combining Eq. (8) with Eq. (7), we easily get

$$\tau_n^0 = \frac{cL^2}{4\pi^2 k}\frac{1}{n^2} \tag{9}$$

In LITG experiments, a sinusoidal TG of wavenumber α_1^0 is initially induced in the sample. Therefore the solution reads

$$T(z,t) = T^{eq} + A\sin(\alpha_1^0 z)e^{-\frac{t}{\tau_1^0}} \tag{10}$$

On the other hand, in AEMD simulations, the initial TG is usually a step-like profile with one half of the simulation box at temperature T_1 and the other half at T_2. Therefore, the relaxation is not rigorously mono-exponential. Nevertheless, being $\tau_n^0 \propto \frac{1}{n^2}$, the higher the order of the harmonic, the shorter its life time and we can approximate the relaxation through a single exponential factor, as discussed below.

In order to describe the thermal equilibration of the periodic profile, in AEMD calculations we need to consider only the difference $\Delta T(t)$ between the average temperatures of the two halves of the system. This difference of temperature reads

$$\begin{aligned}\Delta T(t) &= \frac{2}{L}\int_0^{\frac{L}{2}} T(z,t)dz - \frac{2}{L}\int_{-\frac{L}{2}}^0 T(z,t)dz \\ &= \sum_{n=1}^{\infty}\phi_n e^{-\frac{t}{\tau_n^0}}\end{aligned} \tag{11}$$

The coefficients ϕ_n are proportional to A_n/n (or B_n/n) so that, for a step-like initial temperature profile, we have $\phi_n \propto \frac{1}{n^2}$ as well. Moreover, by considering the expression in Eq. (6), we can state that only the terms with an even value of n give a contribution to the summation. Hence, the second non-zero term in $\Delta T(t)$ has a characteristic time τ_3^0 nine times smaller than the fundamental time τ_1^0. In conclusion, the TG becomes rapidly sinusoidal and the equilibration is matter-of-factly mono-exponential, i.e. after a brief transient the solution in Eq. (10) is recovered.

In practice, knowledge of the leading characteristic time τ_1^0 allows for the determination of the thermal conductivity via Eq. (9) with $n = 1$, i.e. via Eq. (1).

2.2. Bilayer system with ITR

In this section, we generalize the development of Section 2.1 to the case of the bilayer structure shown in Fig. 1-b. A mono-exponential behavior, similar to the bulk case, is recovered and the decay time is related to the thermal response of the interface, i.e. to the ITR.

We define the temperature fields $T^{(1)}(z,t)$ and $T^{(2)}(z,t)$ in the two homogeneous regions of length l_1 and l_2 and conductivity k_1 and k_2 respectively and we consider a mono dimensional heat equation for each region:

$$c_i \frac{\partial T^{(i)}}{\partial t} = k_i \frac{\partial^2 T^{(i)}}{\partial z^2} \tag{12}$$

for $i = 1, 2$, c_i being the volumetric heat capacity of the two materials. According to Kapitza resistance definition, a discontinuity in the temperature field $\delta T = rJ$ is introduced at the interfaces. Therefore, Eq. (12) is solved

with the following set of PBC:

$$T_1(0,t) - T_2(0,t) = rJ(0,t) \tag{13}$$

$$T_2(l_2,t) - T_1(-l_1,t) = rJ_1(-l_1,t) \tag{14}$$

$$J_1(0,t) = J_2(0,t) \tag{15}$$

$$J_1(-l_1,t) = J_2(l_2,t) \tag{16}$$

where the flux J_i are related to the temperature field via Eq. (5). The general solution of Eq. (12) for an arbitrary initial condition reads:

$$T^{(i)}(z,t) = T^{eq} + \sum_{n=1}^{\infty} \theta_n^{(i)}(t)\chi_n^{(i)}(z) \tag{17}$$

where

$$\theta_n^{(i)}(t) = e^{-\frac{t}{\tau_n^{(i)}}} \tag{18}$$

$$\chi_n^{(i)}(z) = a_n^{(i)}\, cos(\alpha_n^{(i)} z) + b_n^{(i)}\, sin(\alpha_n^{(i)} z) \tag{19}$$

and

$$\tau_n^{(i)} = \frac{c_i}{k_i(\alpha_n^{(i)})^2} \tag{20}$$

The allowed wave numbers $\alpha_n^{(i)}$ are eventually obtained by imposing the PBC (13), (14), (15), and (16). The sinusoidal functions $\chi_n^{(i)}(z)$ represent a complete orthonormal basis for the solution of the present problem. As shown in Section 2.1, in the case of a homogeneous system these functions turn out to be the well-known Fourier basis (being $\alpha_n = n\frac{2\pi}{L}$). $a_n^{(i)}$ and $b_n^{(i)}$ are the coefficients of the initial condition in this basis. Moreover, PBC requires that

$$\tau_n^{(1)} = \tau_n^{(2)} = \tau_n \tag{21}$$

This leads to the following relation between the wavenumbers:

$$(\alpha_n^{(1)})^2 \frac{k_1}{c_1} = (\alpha_n^{(2)})^2 \frac{k_2}{c_2} \tag{22}$$

The complete solution is again a superposition of periodic functions of the position damped by exponential functions of the time. Each term of the superposition has a different decay time related to the corresponding wave number by Eq. (20).

For the sake of simplicity, we consider the same bulk properties in the right side and in the left side of the interface (the general case is exposed in Appendix B) and we focus on the interface effects due to the ITR. So, we assume

$$c_1 = c_2 = c \tag{23}$$

$$k_1 = k_2 = k \tag{24}$$

hence, the sets of wavenumbers in the two homogeneous regions coincide

$$\alpha_n^{(1)} = \alpha_n^{(2)} = \alpha_n \tag{25}$$

Moreover, we impose the condition

$$l_1 = l_2 = l = \frac{L}{2} \tag{26}$$

The PBC provide a set of linear equations for the coefficients $a_n^{(i)}$ and $b_n^{(i)}$ involved in the definition of the basis functions $\chi_n^{(i)}(z)$. By imposing that the determinant of this set of equations is zero, we obtain the following transcendental equation for the wavenumber α_n

$$\begin{aligned}(\cos(2l\alpha_n) - 1)\,(rk\alpha_n)^2 + 4\sin(2l\alpha_n) rk\alpha_n \\ -4\,(\cos(2l\alpha_n) - 1) = 0\end{aligned} \tag{27}$$

with the τ_n related to the α_n via Eq. (20), i.e.

$$\alpha_n = \sqrt{\frac{c}{k\tau_n}} \tag{28}$$

It is not possible to solve this equation analytically to find the allowed values of α_n (or τ_n), therefore we cannot write the analytical solution $T^{(i)}(z,t)$. Nevertheless, via Eq. (27), the ITR r can be expressed as a function of the α_n according to

$$r = 2\frac{\sin(2l\alpha_n) + \sqrt{2(1-\cos(2l\alpha_n))}}{(1-\cos(2l\alpha_n))k\alpha_n} \tag{29}$$

This means that knowledge of a single α_n or equivalently of one of the decay times τ_n allows for the calculation of r. Eq. (29) represents, indeed, the main analytical result of the present work.

In the following, we discuss the set of wavenumbers involved in the present problem and we show that, also in the bilayer case, only the longest decay time drives the equilibration of the TG.

First of all, we note that a sequence of solutions of Eq. (27) are obtained for

$$\alpha_n^0 = \frac{\pi n}{l} \tag{30}$$

or, in terms of the decay times, for

$$\tau_n^0 = \frac{cl^2}{k\pi^2}\frac{1}{n^2} \tag{31}$$

These solutions are independent of the value of r and coincide with the decay times (9) of the bulk system. As a matter of fact, they describe the thermal equilibration of components of the initial condition that doesn't require a

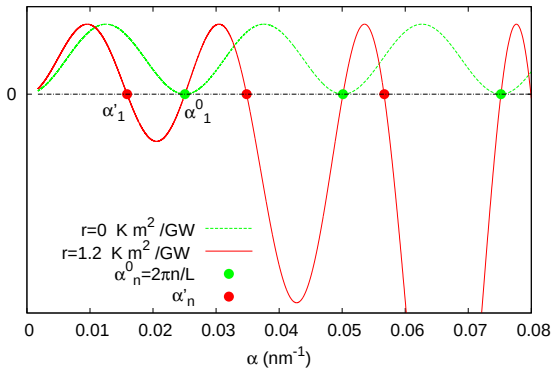

Figure 2: Wavenumbers, obtained via Eq. (27), involved in the solution of the heat conduction problem for a bilayer system in Eq. (17). The curves are the left-hand side of Eq. (27) with $l = L/2 = 125$ nm, $k = 68$ W/mK in the cases $r = 0$ (bulk) and $r = 1.2$ $\mathrm{m}^2K/\mathrm{GW}$ (bilayer). This system is representative of the results obtained in the following sections for the case study considered in the present work, namely a c-Si bilayer system with (100)Σ29 GBs.

heat conduction across the interfaces. In other words, their independence of the interface resistance r implies that they only represent situations where the heat flux across the interfaces is zero. The series of τ_n^0 coincides indeed with the decay times of a system of length L under adiabatic boundary conditions (no heat transfer at boundaries).

In Fig. 2, we report the left-hand side of Eq. (27) as a function of α for the bulk system, i.e. $r = 0$, and for $r = 1.2$ $\mathrm{m}^2\mathrm{K}/\mathrm{GW}$, the intercepts with the horizontal axes supply the corresponding wavenumbers. For $r = 0$ the sequence $\alpha_n^0 = \frac{2\pi n}{L}$ are correctly recovered. As r increases a different sequence of wavenumbers, α_n', is obtained, partially coincident with the $r = 0$ set. Therefore, in the bilayer case ($r \neq 0$) the set of basis function $\chi_n^{(i)}(z)$ may be

split into two subspaces. The first one is composed by sinusoidal functions with wavenumber α_n^0 independent of r and characterized by an heat flux equal to zero at the interfaces. Being the heat flux proportional to the space derivative of the temperature, this subspace is composed by *even* sinusoidal functions. The second subspace, characterized by the wavenumbers α'_n, is therefore composed by *odd* sinusoidal functions.

Hence, for the odd-parity initial condition here considered (see Fig. 1) only the α'_n wavenumbers appear in the solution in Eq.(17). Consequently, only the decay times

$$\tau'_n = \frac{c}{k(\alpha'_n)^2} \tag{32}$$

are considered in the following. The case of an arbitrary initial condition will be discussed in Section 6.

The set of wavenumbers α'_n can be numerically studied, and a good deal of physical insight is gained by defining the normalized wavelength $\frac{\lambda_n}{L}$ and the *normalized Kapitza length* [18] $\frac{kr}{L}$. With these variables, the equation (27) turns into the universal function (i.e. independent of the specific parameters of the problem) plotted in Fig. 3. If the Kapitza length is zero, i.e. in the bulk case where $r = 0$, the Fourier basis wavelengths are recovered, namely $\lambda_n = \frac{L}{n}$. On the other hand, the introduction of the periodic pattern of ITR induces a progressive spread of these wavelengths. In particular, in the limit $rk/L \to \infty$, λ_1 tents to infinity while the others, for $n > 1$, are limited and tent to $\frac{L}{n-1}$. By considering that the decay time τ_n of each component is proportional to λ_n^2, the wavelengths with $n > 1$ turn to be negligible in this limit. Therefore, for high values of the Kapitza length the temperature profile in the bulk regions is flat and the *lumped hypothesis* can be applied.

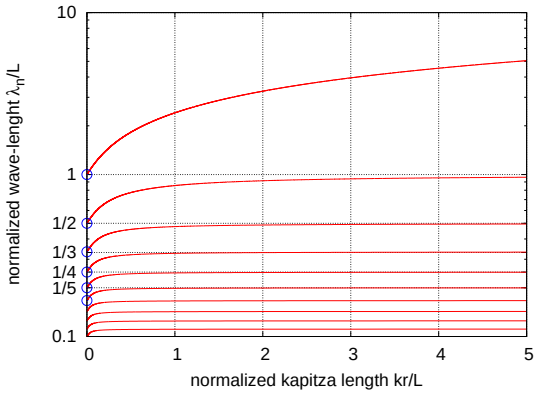

Figure 3: Normalized wavelengths of the base functions for the solution of the heat equation (12) as a function of the normalized Kapitza length (inverse of the Biot number) in the case $l_1 = l_2$ and $k_1 = k_2$.

Indeed the normalized Kapitza length corresponds to the inverse of the Biot number, therefore in the $rk/L \to \infty$ limit the small Biot number regime is recovered.

In Fig. 4, we plot the decay times τ'_n actually involved in Eq. (17) as a function of the ITR r. Clearly, $\tau'_n > \tau^0_n = \tau^0_1/n^2$ for all n and, moreover, for each value of n the difference $\tau'_n - \tau^0_n$ is a decreasing function of n. Therefore, we can state that also in the present bilayer case just one exponential decay times, namely τ'_1, drives the system equilibration, being largely dominant on to the others.

In conclusion, this leading decay time, eventually measured in experiments or obtained by AEMD simulations, allows to extract the value of the ITR by using Eqs. (29) and (28) providing that the bulk conductivity k of the bulk regions is known.

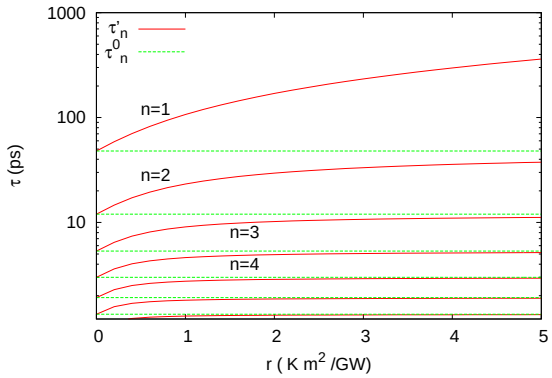

Figure 4: Decay times τ_n of the TG defined in Eqs. (17) and (27) for a bilayer silicon system with period $L = 250$ nm and thermal conductivity $k = 68$ W/mK. In particular we plot the solutions of Eq. (27) as a function of the ITR r.

3. Numerical simulations of a bilayer system

As a straightforward application of the results reported in the previous section, we have applied the AEMD method to the calculation of the interface thermal resistance of a grain boundary (GB) in c-Si. To this aim, the periodic structure in Fig. 1(bottom) has been realized by means of two crystalline slides of the same thickness ($l_1 = l_2 = l$) with different crystallographic orientations joined by a grain boundary. The two slides exhibit the same thermal conductivity ($k_1 = k_2 = k$). Periodic boundary conditions are applied in all the directions, therefore the system is actually composed by two semi infinite layers, parallel to the $x - y$ plane, and two crystallographically identical GBs are present in the supercell. In Appendix A, we report the details of the simulations and the analysis of the atomistic structure of the GBs.

According to the AEMD method, the two halves of these systems have been heated at two different temperature $T_1 = 400$ K and $T_2 = 600$ K so to obtain a initial step-like periodic temperature profile along the z-direction. Afterward, we have let the system equilibrate via a microcanonical simulation. The typical evolution of the TG during the equilibration is plotted in the bottom panel of Fig. 5 while, in the top panel, we show the bulk case for comparison. In both cases, the initial step-like profile rapidly turns into a smooth sinusoidal curve in the two homogeneous regions. In presence of GBs at the interfaces, a jump of the temperature is observed due to their ITR. For the bulk system, the wavenumber of the sinusoidal profile coincides with $\alpha_1^0 = \frac{2\pi}{L}$. In the bilayer case, the profile exhibits a larger wavelength $\lambda_1 = \frac{2\pi}{\alpha_1}$. Coherently with the discussion presented in the previous section, after a brief transient:

$$T^{(i)}(z,t) \simeq T^{eq} + b_1^{(i)} \sin(\alpha_1' z) e^{-\frac{t}{\tau_1'}} \tag{33}$$

In Fig.6, we plot the difference between the average temperatures of the two halves of the systems as a function of the time. In order to exclude the initial multi-exponential behavior and to extract the leading decay time from such a curve, the following fitting procedure have been applied: a mono-exponential and a bi-exponential function have been fitted to the $\Delta T(t)$ data in the range (t_0, t_{max}), t_{max} being the instant when ΔT reaches zero. The left endpoint of the fitting interval, t_0, has been progressively increased. The typical result of the two fitting procedure for the GB calculation is reported in Fig. 7. In particular, the two decay times for the bi-exponential fit and the single decay time for the mono-exponential fit are plotted as a function of t_0. Up to approximately 20 ps, a bi-exponential behavior has been recovered

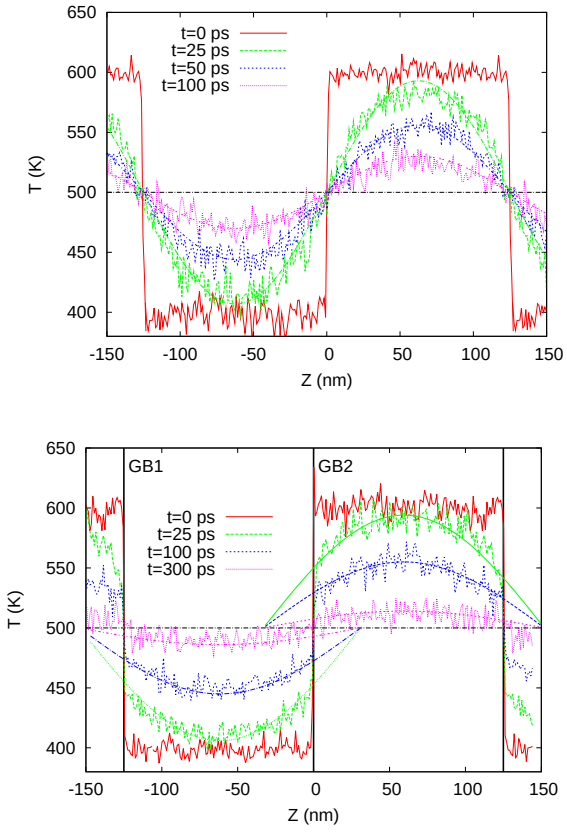

Figure 5: Temperature profiles in a bulk (top panel) and in a bilayer system (bottom panel) during AEMD simulations.

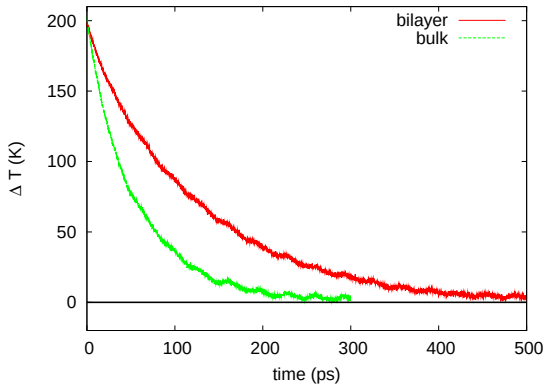

Figure 6: Temporal evolution of the difference of the average temperatures in the two homogeneous regions. In the initial step-like profile, the two regions are equilibrated at $T1$ =400 K and $T2$ =600 K.

with a leading decay time τ_1 of 126.5 ps and a second one, τ_2, 15 to 20 times smaller. After this transient, the second decay time goes to zero and the expected mono-exponential behavior is reached. Consistently, the mono-exponential fit shows a decay time coinciding asymptotically with τ_1. Such a result is in agreement with the analysis of the heat equation solution reported in the previous section and provides a robust fitting procedure to extract the leading decay time from the AEMD simulation.

In order to evaluate the interface resistance from this leading decay time via Eq. (29), the bulk conductivity k is needed. As a matter of fact, at the submicrometric length scale accessible by molecular dynamics, the silicon thermal conductivity depends on the system length. Since the system size is comparable to the phonon mean free paths, the dynamics of a part of the heat carriers is indeed non-diffusive, which affects the effective thermal

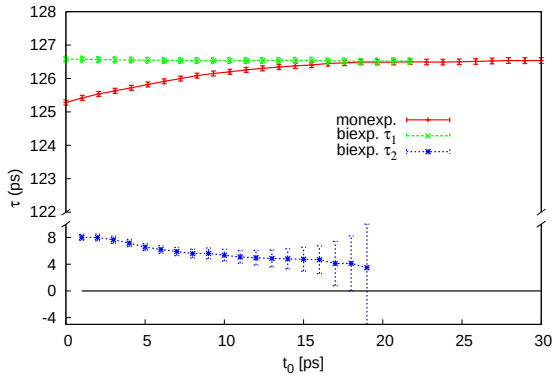

Figure 7: Analysis of the relaxation of a TG in a silicon bilayer system. The simulation results in Fig. 6 are fitted on a mono-exponential function and on a bi-exponential function. The corresponding characteristic times are plotted as function of the left endpoint, t_0, of the fitting interval.

conductivity. Therefore, the value of k in Eq. (29) has to be carefully defined. This could be a purely technical difficulty in the present calculation of the interface resistance since for a material with shorter phonon mean free path such a problem does not occur. However, this issue goes beyond the mere technicality of the choice of the materials, and rather it may represent a crucial point for all studies of thermal properties at the nanoscale based on the classical heat equation. For this reason, in the next section we carefully discuss the size dependence of the bulk conductivity obtained via AEMD.

4. Non-local formulation of the heat transfer

In Fig. 8, we show the AEMD results for the silicon thermal conductivity of our previous work [1]. We have shown that for system sizes in the range

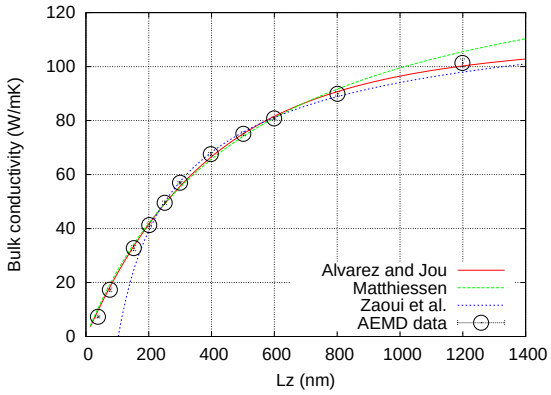

Figure 8: c-Si bulk conductivity at 500 K, obtained via AEMD simulations [1], plotted as a function of the simulation cell length L. The data are fitted by three different analytical models.

[30 nm, 1200 nm] k strongly depends on the length L of the simulation cell. Such an effect is also recovered in MD calculations performed with different techniques. A distinct length-scale dependence is obtained in fact both with non-equilibrium MD approaches (NEMD) and via equilibrium simulations (Green-Kubo). Moreover, in these cases the effective definition of the length-scale parameter is often uncertain [19]. In the NEMD calculations a thermal gradient is induced among a heat source and a heat sink. In between, a region with a linear gradient is identified so to calculate the conductivity as the ratio of the heat flux to the temperature derivative. The result depends on the distance of the source from the sink, but it is not clear if the effective length is the depth of the linear region or rather the source/sink distance.

A similar question arise in AEMD. Does the value of k depend on the simulation cell size L (so it can be considered an artifact of the PBC) or it

Table 1: c-Si bulk conductivity at 500 K calculated via AEMD simulations for different values of the length L of the simulation cell (i.e. of the PBC period) and of the wavelength λ of TG.

λ (nm)	L (nm)	k (W/m/K)
87.3	87.3	22
87.3	174.6	20
87.3	261.9	21
174.4	174.4	36
174.4	348.8	38
250	250	54
250	500	52
350	350	64
350	700	64

depends on the wavelength λ of the TG? In order to answer the question, in table 1 we report the values of k obtained varying both L and λ according to $L = n\lambda$, $n = 1, 2, 3$.

These results clearly prove that the value of k obtained via AEMD depends on the wavelength of the TG λ.

A wavelength dependence of transport parameters at the nanoscale represents a typical deviation from the classical transport theory and it is usually addressed by considering a non-local transport equation. To this aim, a wavenumber dependent conductivity is introduced in the Fourier transform

of Eq. (5)

$$\tilde{J}(\alpha, t) = -i\alpha\tilde{k}(\alpha)\tilde{T}(\alpha, t) \tag{34}$$

where $\alpha = \frac{2\pi}{\lambda}$ is the wavenumber and tilde symbol stands for the Fourier transform

$$\tilde{f}(\alpha) = \int_{-\infty}^{\infty} f(z)e^{-i\alpha z}dz \tag{35}$$

In the macroscopic limit $\lambda \to \infty$, $\tilde{k}(\alpha)$ tends to the macroscopic conductivity k^{∞}. In the real space, Eq. (34) reads

$$J(z, t) = -\int_{-\infty}^{\infty} k(\xi)\frac{\partial T(z-\xi, t)}{\partial z}d\xi \tag{36}$$

where $k(z)$ is an even function representing the non-locality of the thermal transport at the microscopic scale and tents to zero at some distance Δz from origin. Therefore, the property Δz turns to be the actual range of the non-locality. In other words, Eq. (36) states that the heat flux in a given point z depends on the temperature gradient in the neighborhood $(z - \Delta z, z + \Delta z)$ while, in the local formulation, it depends only on the gradient in z. In the macroscopic limit, Δz is negligible, hence $k(z)$ tents to $k^{\infty}\delta(z)$, being $\delta(z)$ the Dirac delta function, and the local Fourier's law is recovered. Eq. (34) leads to the following non-local heat equation

$$c\frac{\partial T(z, t)}{\partial t} = \int_{-\infty}^{\infty} k(\xi)\frac{\partial^2 T(z-\xi, t)}{\partial z^2}d\xi \tag{37}$$

As a consequence of last considerations, the curve in Fig. 8 is naturally interpreted in this contest as the Fourier transform $\tilde{k}(\alpha)$ introduced in Eq. (34).

As reported in the previous section and largely discussed in literature [20, 21], the scale dependence of k is considered a manifestation of the

non-diffusive behavior of heat carriers with a long phonon mean free path and the $k(L)$ curve is usually fitted by the following formula based on the Matthiessen's rule approximation

$$\frac{1}{k(L)} = \frac{1}{k^{\infty}} \left(1 + \frac{L_0}{L}\right) \tag{38}$$

where k^{∞} is the asymptotic (macroscopic) conductivity and L_0 a parameter related to the average phonon mean free path. Eq. (38) is widely adopted to extract the macroscopic conductivity from MD calculations but usually the results strongly depend on the fitting range, at least for materials as crystalline silicon which exhibit long phonon mean free paths. In a precedent paper [21], we proved that the application of this model in AEMD is not fully satisfactory and we proposed a different approximation that better matches the AEMD results at large system sizes, namely:

$$k(L) = k^{\infty} \left(1 + \sqrt{\frac{\Lambda_0}{L}}\right) \tag{39}$$

While this formula has the advantage of providing a very accurate modeling of the values of k at large L, it is however still unsatisfactory since it identifies the length dependence with a merely numerical artifact, namely the size of the simulation supercell.

On the other hand, with the present interpretation of the scale effect in terms of wavelength dependence, a new analytical model can be invoked. Alvarez and Jou [22] indeed, starting from Eq. (36) and applying Boltzmann equation, state the following formula for $\tilde{k}(\lambda)$

$$\tilde{k}(\lambda) = \frac{k^{\infty}\lambda^2}{2\pi^2\lambda_0^2} \left[\sqrt{1 + 4\left(\frac{\pi\lambda_0}{\lambda}\right)^2} - 1\right] \tag{40}$$

Table 2: Results of the fits of the c-Si bulk conductivity, obtained via AEMD simulations, for different analytical models.

model	k^∞ (W/mK)	L_0, Λ_0, λ_0 (nm)
Mathiessen, Eq. (38)	154 ± 6	520 ± 50
Zaoui et al., Eq. (39)	140 ± 2	103 ± 2
Alvarez, Eq. (40)	110 ± 3	135 ± 7

In Fig. 8, the AEMD results are fitted with the three models described above. The Alvarez formula perfectly fits the simulation data on the entire range. The numerical results of the fits of the AEMD data are reported in Table 2.

The macroscopic conductivity k^∞ largely depends on the considered model. We remark that a value of c-Si macroscopic conductivity at 500 K of 154 W/mK coincides with the results usually obtained in MD [23] by means of other techniques but still extrapolated via the Mathiessen formula. On this basis the interatomic potential here adopted, namely the Tersoff potential (see Appendix A), is considered to significantly overestimate the thermal conductivity (experimentally of 80 W/mK at 500 K). We underline that by means of Alvarez formula the macroscopic conductivity predicted by AEMD (110 W/mK) is closer to the experimental value than the other estimations. This means that probably the Tersoff potential is not so inadequate to a quantitative study of the thermal transport in silicon. Moreover, important variations of the extrapolated value can be obtained by varying the range of the fit, namely of 22% for the Matthiessen formula, of 19% for the Zaoui et

al. and 8% for Alvarez formula.

The present results show that the Alvarez formula, developed in the contest of non-local thermal transport, seems to be the best suited to model the AEMD data. This confirms one of the main results of this work: the thermal transport in dielectric materials at the nanoscale can be modeled by the classical heat equation providing that a non-local formulation is considered. The non-local thermal conductivity, both in α-space and in z-space are shown in top panel and in bottom panel of Fig. 9 respectively. The $\tilde{k}(\alpha)$ curve has been obtained by means of Eq. (40) with the parameters in Table 2. The corresponding curve in the z-space, obtained by numerical integration, shows that the range of the non-locality Δz is approximately 50 nm.

Actually, the non-local formulation of the heat transfer induces a different analytical modeling of the AEMD simulations. Namely, in Section 2, Eqs. (2) and (5) have to be replaced by Eqs. (37) and (36), respectively. In Appendix B, we show that in spite of the modification of the analytical model, the main results of Section 2 are still valid if the constant bulk conductivity k is replaced by the its non-local counterpart $\tilde{k}(\alpha)$.

5. AEMD calculation of the grain boundary thermal resistance

In Section 3, we shown how to extract the leading decay time τ_1' from AEMD simulations of a bilayer system of periodicity L. In order to calculate the corresponding interface thermal resistance r via Eq. (29), the value of the bulk conductivity is needed. In the above Section, we have seen that the bulk conductivity is actually a function of the wavenumber α of the TG. As a consequence, in the precedent analytical results, k must be replaced by

$\tilde{k}(\alpha)$. In particular, Eq. (29) reads

$$r = 2\frac{\sin(2l\alpha) + \sqrt{2(1-\cos(2l\alpha))}}{(1-\cos(2l\alpha))\tilde{k}(\alpha)\alpha} \tag{41}$$

$$\tag{42}$$

where $\tilde{k}(\alpha)$ is given by the Alvarez formula

$$\tilde{k}(\alpha) = \frac{2k^{\infty}}{(\alpha\lambda_0)^2}\left[\sqrt{1+(\alpha\lambda_0)^2} - 1\right] \tag{43}$$

with parameters fitted on the AEMD data for the bulk system. The value of α is obtained from the τ_1' according to

$$\tau_1' = \frac{c}{\tilde{k}(\alpha)\alpha^2} \tag{44}$$

i.e. to

$$\alpha = \frac{c}{k^{\infty}\tau_1'}\left(1 + \frac{\lambda_0^2 c}{4k^{\infty}\tau_1'}\right) \tag{45}$$

if $\tilde{k}(\alpha)$ in Eq. (43) is assumed.

In other words, in the non-local formulation of the heat transfer, the effective bulk conductivity of a bilayer system of periodicity L is given by the conductivity at the wavelength $\lambda_1 = \frac{2\pi}{\alpha_1}$ (greater than L) solution of Eq. (27) and related to the decay time τ_1' by Eq. (44).

An empirical proof of the coherence of this statement can be obtained by calculating the values of k by Eq. (44), i.e.

$$k = \frac{c\lambda^2}{\tau_1' 4\pi^2} \tag{46}$$

with both τ_1' and λ extracted from the MD simulations of the bilayer system. Indeed, the wavenumber, and therefore λ, can be directly extracted from the simulated TG (see Fig. 5). In Table 3, we report the results of this analysis.

Table 3: Values of the decay time τ_1' and of the wavelength λ of the temperature profile extracted from numerical simulations of the bilayer system (see bottom panel of Fig. 5) for different values of the TG period L.

L (nm)	τ_1' (ps)	λ (nm)	k via Eq.(46) (W/m/K)	$k(\lambda)$ via Eq.(43) (W/m/K)
32.7	25	90	17	26
87.3	48	180	35	41
150	77	285	55	55
250	126	390	64	68
400	218	575	79	81
600	798	790	90	88

For different values of the system size L, we show the corresponding decay time τ_1' and wavelength λ deduced from the simulations. The effective value of k is then calculated via Eq. (46). Finally, in the Table we show the values of $k(\lambda)$ obtained in the bulk simulations.

These data show that the effective conductivity $\tilde{k}(\alpha)$ calculated via Eq. (46) with τ_1' and λ extracted from the AEMD simulation of the bilayer system coincides with the conductivity of the bulk at this wavelength λ (minor discrepancies are due to the rough estimation of λ supplied by the fitting of the noisy and time depend temperature profile obtained in the simulations). This analysis substantiates the application of the non-local heat equation in the numerical evaluation of the ITR at the nanoscale.

In Fig. 10, we plot the ITR of the c-si GB calculated via Eqs. (46), (43),

and (45) with the values of τ_1' deduced from AEMD simulations of bilayer systems of different periodicity L. A size dependence of the ITR is observed up to approximately 200 nm. On the other hand, the asymptotic value (1.2 m^2K/GW) is in good agreement with the value obtained by Schelling *et al.* [24] and by other authors [25] by means of the NEMD technique.

The interface thermal resistance is an inherently local property, therefore a scale effect is in principle unexpected. Other works [26, 27] have found such a scale dependence in ITR numerical calculations. This artifact has been associated to the effects of the ballistic phonon transport. As discussed in Section 4, in the present formulation non-diffusive effects are taken into account by the non-local modeling of the heat transfer of the bulk. Nevertheless, the non-local conductivity $k(\xi)$, here adopted for the interpretation of the heat transfer in presence of ITRs, doesn't account for the presence of these inhomogeneities. The $k(\xi)$ curve, shown in the bottom panel of Fig. 9, represents indeed an homogeneous non-locality relating the heat flux in a given point to the derivative of temperature at a distance ξ (see Eq. (34). When an interface is present at this distance, the smooth $k(\xi)$ function is no longer appropriate. A more advanced model could in principle be conceived with a more general non homogeneous kernel function $k(z, z')$, in spite of the present homogeneous kernel $k(z' - z)$. Nevertheless, in Fig. 9, we can observe that the range of the non-locality, Δz, is around 50 nm. Therefore, the present homogeneous approximation is admissible when the distance between the interfaces sufficiently exceeds this limit. As a matter of fact, beyond 200 nm the obtained value of the ITR is constant and it coincides with the result available in literature. This means that, above this

threshold, the homogeneous kernel correctly describes the heat transport in this nanostructure. We remark that, up to at least 1200 nm, the ballistic effects are still prominent (see Fig. 8). Hence, we state that in this range the present non-local formulation is able to model the ballistic effects in bilayer silicon systems.

In this section, we shown that AEMD technique can be efficiently applied to the numerical evaluation of ITRs, also in presence of non diffusive effects. In the contest of the atomistic simulation, several methods exist to study the thermal behavior of the interfaces. Nevertheless, they often assume the lamped approximation, namely a constant temperature profile into the bulk regions. The AEMD method doesn't require this approximation and, exploiting transient phenomena, it is a time-saving approach able to address the interface thermal conduction at the nanoscale.

6. Experimental application

The experimental study of the thermal transport in nanostructures with possible observations of non-diffusive phenomena, is a very challenging task. Several techniques are usually applied as the Raman thermometry [28], 3ω method [29, 30], time-domain thermo-reflectance [31] or scanning thermal microscopy. Nevertheless, important limitations are however present. These methods often work in the optical regime with a consequently reduced spatial resolution. Device-based approach or other methods which adopt metallic heaters in thermal measurements, couple the sample to extraneous structures. This induces additional difficulties in the extrapolation of the thermal properties of the sample from the response of the overall system, especially

in the case of non-diffusive transport.

On the other hand, the LITG technique offers a non-invasive approach to the thermal studies allowing for a high accuracy and reproducibility of the results. Moreover, the thermal response is obtained as a function of wavelength of the TG, i.e. the period of the grating, therefore non-local effects can be directly detected. Indeed, by means of this experimental technique, a non-diffusive behavior revealed by a grating wavelength dependence has been already verified in silicon membranes [7, 32]. In this case the scale effect is due to the nanometric thickness of the structure and it is obtained for grating periods in the micrometer scale.

In the above Sections, we showed how to apply the present model in AEMD simulations in order to predict the thermal behavior of interfaces. Since the AEMD is the straightforward numerical counterpart of the LITG technique, a similar setup could be implemented in this experimental approach, opening the way to a direct measurement of interfaces thermal resistances.

One of the first difficulties in the experimental implementation of the present model is the generation of TG with a sufficiently short wavelengths. In order to obtain a significant thermal effect of the interfaces, indeed, the spatial period of the structure, and consequently of the thermal grating, have to be comparable to the Kapitza length rk of the interface. For silicon grain boundaries, the present work shows that the Kapitza length is about 100 nm. Actually, the standard LITG techniques are performed in the optical regime, therefore the wavelengths are limited to the microscale. Nevertheless, recent advances in laser physics based on four-wave mixing processes allow

for shorter wavelengths thermal gratings, i.e. in the extreme ultraviolet and soft-X-ray ranges [33].

Furthermore, the interface resistance calculation strongly depends on the knowledge of the conductivity of the surrounding bulk. Therefore, an accurate experimental determination of the effective k in the bulk material is required. To address this last issue, we study here the effect of a possible phase shift between the periodic multilayer structure and the laser induced TG (see Fig. 11). We show that a variable phase shift can be exploited to define a unified measurement protocol for both conductivities and interface thermal resistance.

We performed AEMD simulations on the bilayer system by considering a shift L_s of the temperature profile with respect to grain boundaries positions, as shown in Fig. 11. When $L_s = 0$, the GBs lies on the zeros of the sinusoidal temperature profile and the TG is an odd function. This is the *in-phase* configuration adopted so far. If $L_s = \frac{L}{4}$, the GBs lies on the maximum/minimum of the profile and the TG is an even function in *quadrature* with respect to the periodic structure. Finally, if $L_s = \frac{L}{2}$, the configuration is equivalent to the in-phase case being just the cold and hot regions exchanged. The in-phase configuration has been discussed in the previous Sections, the leading decay time is τ_1' and it is related to the ITR by Eq. (29). Conversely, in the quadrature configuration the heat flux at the GBs is zero and hence there is no discontinuity in the temperature profile (see Fig. 12). As a consequence, in this particular case, the ITR doesn't have any effect on the relaxation and the bulk leading decay time τ_1^0 have to be recovered. This consideration has been mentioned in Section 2.2 in order to

discuss the two sequences of solutions, $\{\alpha_n^0\}$ and $\{\alpha_n'\}$, of Eq. (27).

In Fig. 13, we report the analysis of the relaxation calculated in AEMD simulations as function of the phase shift L_s. The results fully confirm the above picture. In the top panel we show the leading decay time of the temperature difference $\Delta T(t)$ which varies in the range (τ_1^0, τ_1'). In the bottom panel of Fig. 13, we show the results of the fit of $\Delta T(t)$ curves according to

$$\Delta T(t) = C_0 e^{-\frac{t}{\tau_1^0}} + C_1 e^{-\frac{t}{\tau_1'}} \tag{47}$$

Consistently with the analytical model developed in Section 2.2, these results show that, when the TG and the periodic structure are in-phase, the relaxation is mono exponential with a decay time τ_1'. While, for $L_s \in (0, \frac{L}{4})$, the relaxation is a linear combination of two components, one with a bulk-like time decay τ_1^0 and the other with the ITR-dependent decay time τ_1'. When $L_s = \frac{L}{4}$ just the bulk-like component is present. With respect to experimental application, this means that a variable phase shift sweep the leading decay time from a *minimum value* τ_1^0, required to calculate k through Eq. (31), to a *maximum value* τ_1', required to obtain r through Eq. (29). Therefore, by varying the phase shift the same experiment can in principle predict the effective conductivity of the bulk regions and the interface thermal resistance of the non-homogeneous sample.

7. Conclusions

In this work, we firstly developed a generalization of the classical Sommerfeld heat-conduction problem on a ring, by introducing non-ideal interfaces described by Kapitza thermal resistances. The solution of this problem allows to relate the interface thermal resistance to the decay time of a thermal

grating. Moreover, the application of the model at the nanoscale required a non-local formulation of the heat transfer in order to take into account non-diffusive effects in materials with a long phonon mean free path. In particular, we introduced an homogeneous non-local bulk conductivity in the diffusive heat equation to model the scale dependence of the thermal behavior of the bulk. This strategy allows to correctly describe the non-diffusive effects in thermal transport at the nanoscale at least down to a lower limit (about 200 nm for silicon).

The relaxation of a TG in a bulk material is already applied both in numerical techniques (AEMD) and in experimental approaches (LITG) in order to calculate the thermal conductivity. With the present results, we extend the AEMD method to the calculation of interface thermal resistances and we suggest a protocol to measure this property in LITG experiments. As a numerical case study, we have calculated the interface thermal resistances of a silicon grain boundary. The value obtained with the present AEMD method is in agreement with the available results. Some aspect of the possible experimental application of the present model have been discussed and a protocol to obtain both bulk and interface contribution to the heat transfer in a same sample has been proposed.

Since the AEMD is the numerical counterpart of the LITG experimental technique, exactly the same setup can by implemented in both the approaches. Therefore, a straightforward comparison between the corresponding results can efficiently increase the physical understanding of the heat transport in heterogeneous structures. In conclusion, such a non-invasive et non-destructive LITG approach, joined to its numerical counterpart, deserves

experimental investigation for both fundamental physics and applications.

Appendix A. Simulation details and grain boundary models

In this work, we considered the disordered (100)Σ29 twist grain boundary in silicon. The thermal behavior of this high energy GB as been addressed by several previous works [24, 34]. Moreover, the average GB thermal resistance of polycrystalline silicon evaluated via MD simulation [35] is very similar to that of (100)Σ29. Therefore, this grain boundary structure has been considered as a representative model of a generic GB in polycrystalline Si.

In all the simulations (performed with a modified version of the DL_POLY 4 package [36]), the interaction between silicon atoms has been modeled by the Tersoff potential [37]. The x and y dimensions have been fixed at 62.24 nm corresponding to the equilibrium lattice constants of the perfect crystals at the temperature $T^{eq} = 500$ K. This temperature, close to the Debye temperature of silicon, has been considered as the reference temperature for our MD calculations of the thermal properties of this material.

In order to check the dependence of the results on the atomistic model of the interface, two microscopically different structures of the grain boundary have been achieved by means of a treatment similar to that presented by Keblinski *et al* [38, 39] for silicon systems modeled by the Stillinger-Weber potential. Firstly, a zero temperature equilibrium structure has been obtained by static iterative energy minimization and then relaxed at 500 K (*ordered GB*). Then, a disordered lower energy structure (*annealed GB*) has been obtained by thermal annealing at 2000 K, namely 400 K below the melting temperature of silicon simulated via the Tersoff potential. In order

Table A.4: : Leading decay times calculated via AEMD simulation of the two different models of GB.

L (nm)	τ annealed GB (ps)	τ ordered GB (ps)
32.7	25	24
87.3	48	49.5
150	77	76
250	126	130
400	218	215.5

to promote configurational transformations of the GB structure, during the simulations a constant stress algorithm in the direction orthogonal to the GB surface has been applied.

For both the GB models, in Fig. A.14 we plot the energy per atom of the atomic layers parallel to the GB surface and a snapshot of the atomic structure at $T = 0$ of the two models of GB. The annealing process has allowed a reduction of the GB energy from 1592 erg/cm^2 of the ordered GB to 1409 erg/cm^2 of the annealed GB, corresponding to a decrease of 11%. These results are very similar to those obtained by Keblinski *et al* [38] with the StillingerWeber Potential, namely 1464 erg/cm^2 and 1300-1340 erg/cm^2, corresponding to a reduction of approximately 10%.

In spite of the quite significant structural difference between the two models, the results of the AEMD calculations, reported in Table A.4, are not remarkably dissimilar.

Therefore, only the results obtained by the annealed GB model are dis-

cussed in the paper.

Appendix B. Non-local heat conduction problem on a ring

We consider here the non-local heat equation (37). The general solution can be calculated by separation of variables. The temperature field is therefore expressed by

$$T(z,t) = \chi(z)\phi(t) \tag{B.1}$$

and Eq. (37) reads

$$c\frac{\partial\phi(t)}{\partial t}\frac{1}{\phi(t)} = \frac{1}{\chi(t)}\int_{-\infty}^{\infty} k(\xi)\frac{\partial^2\chi(z-\xi)}{\partial z^2}d\xi \tag{B.2}$$

As a consequence, $\chi(z)$ and $\phi(t)$ verify the following equations:

$$\frac{\partial\phi(t)}{\partial t} = -\frac{\beta^2}{c}\phi(t) \tag{B.3}$$

$$\int_{-\infty}^{\infty} k(\xi)\frac{\partial^2\chi(z-\xi)}{\partial z^2}d\xi = -\beta^2\chi(t) \tag{B.4}$$

where β is a arbitrary constant. Eq. (B.3) states that

$$\phi(t) \propto e^{-\frac{t}{\tau(\beta)}} \tag{B.5}$$

where

$$\tau(\beta) = \frac{c}{\beta^2} \tag{B.6}$$

In order to solve Eq. (B.4), we consider the Fourier transform of $\chi(z)$ and $k(z)$ and we obtain

$$\tilde{\chi}(\alpha)\left(1 - \frac{\alpha^2}{\beta^2}\tilde{k}(\alpha)\right) = 0 \tag{B.7}$$

where α is the wavenumber of the Fourier transform. $k(z)$ is an even function, hence $\tilde{k}(\alpha) = \tilde{k}(-\alpha)$ and

$$\tilde{\chi}(\alpha) = \delta\left(\alpha \pm \sqrt{\frac{\beta^2}{\tilde{k}(\alpha)}}\right) \tag{B.8}$$

Finally, we get

$$\chi(z) = Ce^{i\alpha z} + C^* e^{-i\alpha z} \tag{B.9}$$

where C is an arbitrary complex constant and $\alpha^2 = \frac{\beta^2}{\tilde{k}(\alpha)}$. Combining this last equation with Eq. (B.6), we obtain

$$\tau = \frac{c}{\alpha^2 \tilde{k}(\alpha)} \tag{B.10}$$

equivalent to Eq. (7).

Appendix B.1. Periodic boundary conditions for a bulk system

In Eq. (B.9), the allowed values of the wavenumber α are defined by the boundary conditions. We firstly take into consideration the PBC in Eqs. (3) and (4) defining a periodic homogeneous system. The non-locality of the model affects the definition of the heat flux according to Eq. (36) and leads to following set of PBC

$$T(0,t) = T(L,t) \tag{B.11}$$

$$\int_{-\infty}^{\infty} k(\xi) \frac{\partial T(-\xi,t)}{\partial z} d\xi = \int_{-\infty}^{\infty} k(\xi) \frac{\partial T(L-\xi,t)}{\partial z} d\xi \tag{B.12}$$

By replacing Eq. (B.9) in these last equations, we find that solutions exist for all C_1 if $e^{i\alpha L} = 1$, hence

$$\alpha_n = \frac{2\pi n}{L} \tag{B.13}$$

Therefore, we prove that the non-local formulation just introduce the wavelength dependent conductivity $\tilde{k}(\alpha)$ in the solution for the bulk case reported in Section 2.1.

Appendix B.2. Periodic boundary conditions for a bilayer system

We consider now the set of PBC, involving ITRs, in Eqs. (13), (14), (15), and (16). In the present non-local formulation, the heat flux reads

$$J_i(z,t) = -\int_{-\infty}^{\infty} k_i(\xi)\frac{\partial T_i(z-\xi,t)}{\partial z}d\xi \tag{B.14}$$

The PBC equations admit solution in the case $\tau^{(1)} = \tau^{(2)}$, i.e.

$$\frac{c_1}{\alpha_1^2\tilde{k}_1(\alpha_1)} = \frac{c_2}{\alpha_2^2\tilde{k}_2(\alpha_2)} \tag{B.15}$$

Moreover, the wavenumbers in Eq. (B.9) are provided, in this case, by

$$\Psi^+ \sin(\alpha_1 l_1 + \alpha_2 l_2) \tag{B.16}$$

$$+ \quad \Psi^- \sin(\alpha_1 l_1 - \alpha_2 l_2)$$

$$+ \quad \Omega^+\Xi^+ \cos(\alpha_1 l_1 + \alpha_2 l_2) \tag{B.17}$$

$$+ \quad \Omega^-\Xi^- \cos(\alpha_1 l_1 - \alpha_2 l_2) + 4 = 0 \tag{B.18}$$

where

$$\Psi^+ = 2r\left(\alpha_1\tilde{k}_1(\alpha_1) + \alpha_2\tilde{k}_2(\alpha_2)\right) \tag{B.19}$$

$$\Psi^- = 2r\left(\alpha_1\tilde{k}_1(\alpha_1) - \alpha_2\tilde{k}_2(\alpha_2)\right) \tag{B.20}$$

$$\Omega^+ = \left(\alpha_2\tilde{k}_2(\alpha_2)r + \frac{\alpha_2\tilde{k}_2(\alpha_2)}{\alpha_1\tilde{k}_1(\alpha_1)} + 1\right) \tag{B.21}$$

$$\Xi^+ = \left(\alpha_1\tilde{k}_1(\alpha_1)r - \frac{\alpha_1\tilde{k}_1(\alpha_1)}{\alpha_2\tilde{k}_2(\alpha_2)} - 1\right) \tag{B.22}$$

$$\Omega^- = -\left(\alpha_2\tilde{k}_2(\alpha_2)r - \frac{\alpha_2\tilde{k}_2(\alpha_2)}{\alpha_1\tilde{k}_1(\alpha_1)} + 1\right) \tag{B.23}$$

$$\Xi^- = \left(\alpha_1\tilde{k}_1(\alpha_1)r - \frac{\alpha_1\tilde{k}_1(\alpha_1)}{\alpha_2\tilde{k}_2(\alpha_2)} + 1\right) \tag{B.24}$$

If, in this last equation, we take $l_1 = l_2$ and $k_1 = k_2$, we recover Eq. (27) of Section 2.2 with the non-local conductivity $\tilde{k}(\alpha)$ in spite of the macroscopic one. Therefore, also the results of Section 2.2 are still valid in the non-local formulation providing that the macroscopic bulk conductivity k is replaced by its non-local counterpart $\tilde{k}(\alpha)$. Finally, Eq. (B.24) represents the generalization of Eq. (27) to the case $l_1 \neq l_2$ and $k_1 \neq k_2$.

References

[1] E.Lampin, P. L. Palla, P.-A. Francioso, and F. Cleri, Thermal conductivity from approach-to-equilibrium molecular dynamics, J. Appl. Phys. **114**, 033525 (2013).

[2] H.J. Eichler, P. Gunter and, DW.Pohl, *Laser-Induced Dynamic Gratings* (Springer, New York, 1986)

[3] A. A. Maznev, J . A .Johnson, and K. A. Nelson, Onset of non-diffusive phonon transport in transient thermal grating decay, Phys. Rev. B **84**, 195206 (2011)

[4] L.D. Landau and E.M. Lifshitz, Theory of Elasticity, Volume 7 of A Course of Theoretical Physics, (Pergamon Press 1970)

[5] M. Herzog, D. Schick, P. Gaal, R. Shayduk, C. von Korff Schmising, and M. Bargheer., Analysis of ultrafast X-ray diffraction data in a linear-chain model of the lattice dynamics Appl. Phys. A **106**, 489 (2012).

[6] R. Shayduk, H. A. Navirian, W. Leitenberger, J. Gold- shteyn, I. Vrejoiu, M. Weinelt, P. Gaal, M. Herzog, C. von Korff Schmising, and

M. Bargheer, Nanoscale heat transport studied by high-resolution time-resolved x-ray diffraction, New J. Phys. **13**, 093032 (2011).

[7] A. Vega-Flick, R. A. Duncan, J. K. Eliason, J. Cuffe, J. A. Johnson, J.-P. M. Peraud, L. Zeng, Z. Lu, A. A. Maznev, E. N. Wang, J. J. Alvarado-Gil, M. Sledzinska, C. M. Sotomayor Torres, G. Chen, and K. A. Nelson, Thermal transport in suspended silicon membranes measured by laser-induced transient gratings, AIP Advances **6**, 121903 (2016).

[8] A. Stampanoni Panariello, B. Hemmerling, and W. Hubschmid, Electrostrictive generation of nonresonant gratings in the gas phase by multimode lasers, Phys. Rev A **51**, 655 (1995).

[9] C. Melis and L. Colombo, Lattice Thermal Conductivity of $Si_{1x}Ge_x$ Nanocomposites, Phys. Rev. Lett.**112**, 065901 (2014).

[10] M. Royo and R. Rurali, Tuning thermal transport in Si nanowires by isotope engineering, Phys. Chem. Chem. Phys. **18**, 26262 (2016).

[11] Y. Chen, Y. Zhang, K. Cai, J. Jiang, J.-C. Zheng, J. Zhao, and N. Wei., Interfacial thermal conductance in graphene/black phosphorus heterogeneous structures, Carbon, **117**, 399-410 (2017).

[12] T. B. Limbu, K. R. Hahn, F. Mendoza, S. Sahoo, J. J. Razink, R. S. Katiyar, B. R. Weiner, and G. Morell, Grain size-dependent thermal conductivity of polycrystalline twisted bilayer graphene, Carbon **117**, 367-375 (2017).

[13] A. Bouzid, H. Zaoui, P.L. Palla, G. Ori, M. Boero, C. Massobrio, F. Cleri, and Evelyne Lampin, Thermal conductivity of glassy GeTe4 by

first-principles molecular dynamics, Phys. Chem. Chem. Phys. **19**:15, 9729-9732 (2017).

[14] F. Pavanello, F. Manca, P. L. Palla, and S.Giordano, Generalized interface models for transport phenomena: Unusual scale effects in composite nanomaterials, J. Appl. Phys. **112**, 084306 (2012).

[15] P. L. Kapitza, Collected Papers of P. L. Kapitza (Pergamon, Oxford, 1964), Vol. 3.

[16] A. Sommerfeld, Lectures on Theoretical Physics. Vol. 6. Partial Differential Equations in Physics (Academic Press 1949).

[17] I.R. Vengerov, Generalization of Sommerfeld heat-conduction problem for a ring, J. Eng. Phys **35**, 866 (1978).

[18] J-L Barrat and F. Chiaruttini, Kapitza resistance at the liquidsolid interface, Molecular Physics **101**, 1605 (2003).

[19] P.C. Howell, Thermal Conductivity Calculation with the Molecular Dynamics Direct Method I: More Robust Simulations of Solid Materials, J. Comput. Theor. Nanosci.**8**, 2129 (2011)

[20] D. P. Sellan, E. S. Landry, J. E. Turney, A. J. H. McGaughey, and C. H. Amon1, Size effects in molecular dynamics thermal conductivity predictions, Phys. Rev. B **81**, 214305 (2010)

[21] H. Zaoui, P. L. Palla, F. Cleri, and E. Lampin, Length dependence of thermal conductivity by approach-to-equilibrium molecular dynamics, Phy. Rev.B, **94**, 054304 (2016).

[22] F. X. Alvarez and D. Jou, Memory and nonlocal effects in heat transport: From diffusive to ballistic regimes, Appl. Phys. Lett. **90**, 083109 (2007).

[23] P. C. Howell, Comparison of molecular dynamics methods and interatomic potentials for calculating the thermal conductivity of silicon, J. Chem. Phys. **137**, 224111 (2012).

[24] P. K. Schelling, S. R. Phillpot and P. Keblinski, Kapitza conductance and phonon scattering at grain boundaries by simulation, J. Appl. Phys. **95**, 6082 (2004).

[25] Jan K. Bohrer, Kevin Schrer, Lothar Brendel, and Dietrich E. Wolf, Thermal resistance of twist boundaries in silicon nanowires by nonequilibrium molecular dynamics, AIP Advances **7**, 045105 (2017).

[26] Zhi Liang, Kiran Sasikumar, and Pawel Keblinski, Thermal Transport across a SubstrateThin-Film Interface: Effects of Film Thickness and Surface Roughness, Phys. Rev. Lett. **113**, 065901 (2014).

[27] Zhi Liang, and Pawel Keblinski, Finite-size effects on molecular dynamics interfacial thermal-resistance predictions, Phys. Rev.B **90**, 075411 (2014).

[28] J. S. Reparaz, E. Chavez-Angel, M. R. Wagner, B. Graczykowski, J. Gomis-Bresco, F. Alzina1, and C. M. Sotomayor Torres, A novel contactless technique for thermal field mapping and thermal conductivity determination: Two-Laser Raman Thermometry, Rev. Sci. Inst. **85**, 034901 (2014).

[29] D.G.Cahill and R.O. Pohl, Thermal conductivity of amorphous solids above the plateau, Phys. Rev. B **35**, 40674073 (1987).

[30] D.G. Cahill, Thermal conductivity measurement from 30 to 750 K: the 3 method, Rev. Sci. Inst. **61**, 802 (1990).

[31] D.G. Cahill, W. K. Ford, K. E. Goodson, G. D. Mahan, A. Majumdar,H. J. Maris, R. Merlin, S. R. Phillpot, Nanoscale thermal transport, J. Appl. Phys. **93**, 793 (2003).

[32] Jeremy A. Johnson, A. A. Maznev, John Cuffe, Jeffrey K. Eliason, Austin J. Minnich, Timothy Kehoe, Clivia M. Sotomayor Torres, Gang Chen, and Keith A. Nelson, Direct Measurement of Room-Temperature Nondiffusive Thermal Transport Over Micron Distances in a Silicon Membrane, Phys. Rev. Lett. 110, 025901 (2013).

[33] F. Bencivenga, R. Cucini, F. Capotondi, A. Battistoni, R. Mincigrucci, E. Giangrisostomi, A. Gessini, M. Manfredda, I. P. Nikolov, E. Pedersoli, E. Principi, C. Svetina, P. Parisse, F. Casolari, M. B. Danailov, M. Kiskinova, and C. Masciovecchio, Four-wave mixing experiments with extreme ultraviolet transient gratings, Nature **502**, 205 (2015).

[34] T. Watanabe, B. Ni, S. R. Phillpot, P. K. Schelling and P. Keblinski, Thermal conductance across grain boundaries in diamond from molecular dynamics simulation, J. Appl. Phys. **102**, 063503 (2007)

[35] S. H. Ju and X. G. Liang, Thermal rectification and phonon scattering in asymmetric silicon nanoribbons, J. Appl. Phys. **112**, 064305 (2012).

[36] I. T. Todorov and W. Smith, The DL_POLY 4 User Manual (Daresbury Lab).

[37] J. Tersoff, Empirical interatomic potential for silicon with improved elastic properties, Phy. Rev. B **38**, 9902 (1988).

[38] P. Keblinski, S. R. Phillipot, D. Wolf, and H. Gleiter, Thermodynamic Criterion for the Stability of Amorphous Intergranular Films in Covalent Materials, Phys. Rev. Lett. **77**, 2965 (1996).

[39] P. Keblinski, S. R. Phillpot, and D. Wolf, and H. Gleiter On the Thermodynamic Stability of Amorphous Intergranular Films in Covalent Materials, J. Am. Ceram. Soc . **80**, 717 (1997)

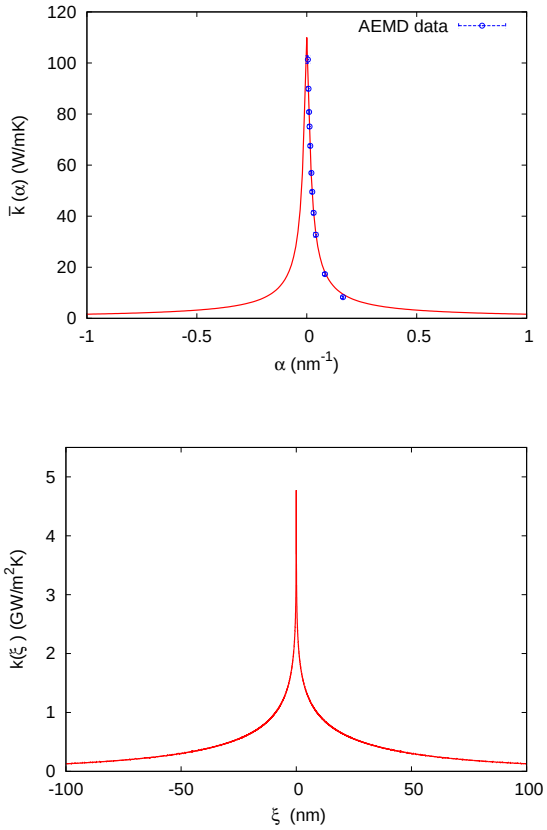

Figure 9: Non-local thermal conductivity $\tilde{k}(\alpha)$ calculated in AEMD simulations (top panel), the continuous line has been obtained by fitting the data on the Alvarez formula in Eq. (40). In the bottom panel, we report the corresponding Fourier transform

.

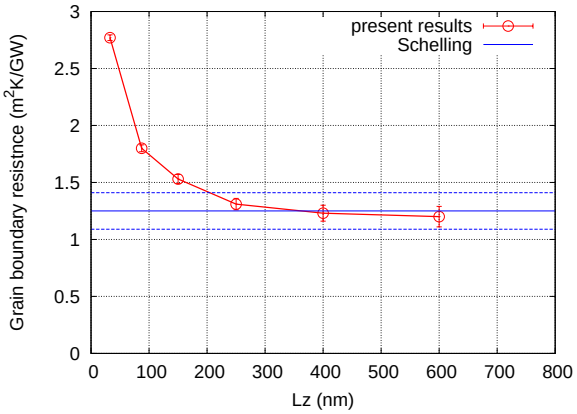

Figure 10: GB thermal resistance calculated via AEMD method.

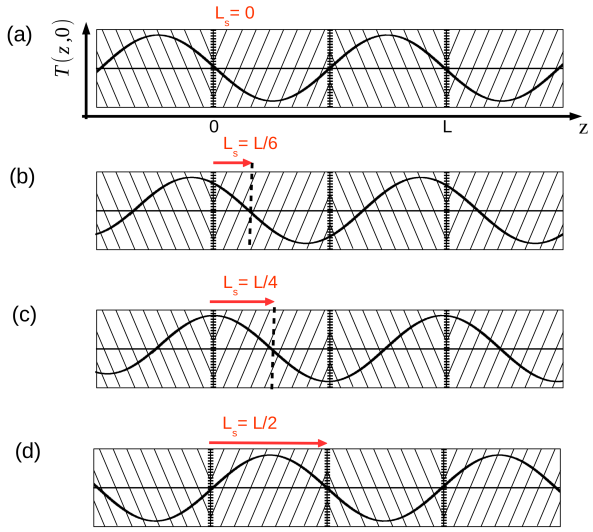

Figure 11: Different phases of the TG with respect to the periodic structure of the system. The parameter L_s represents the relative shift: $L_s = 0$ (panel a) corresponds to the in-phase configuration, $L_s = \frac{L}{4}$ (panel c) to the the quadrature configuration. For $L_s = \frac{L}{2}$ the configuration is equivalent to the in-phase one.

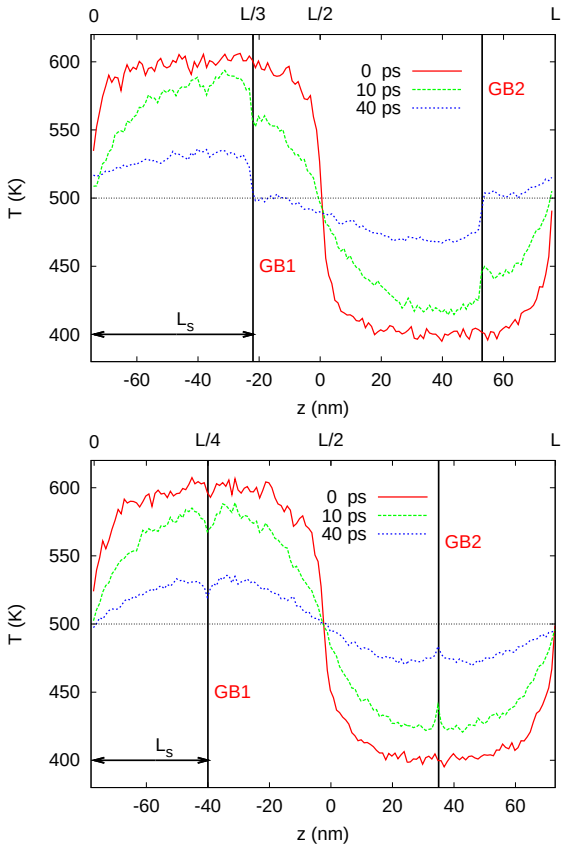

Figure 12: Relaxation of the temperature profile in the bilayer system in case of a phase shift between the TG and the periodic structure.

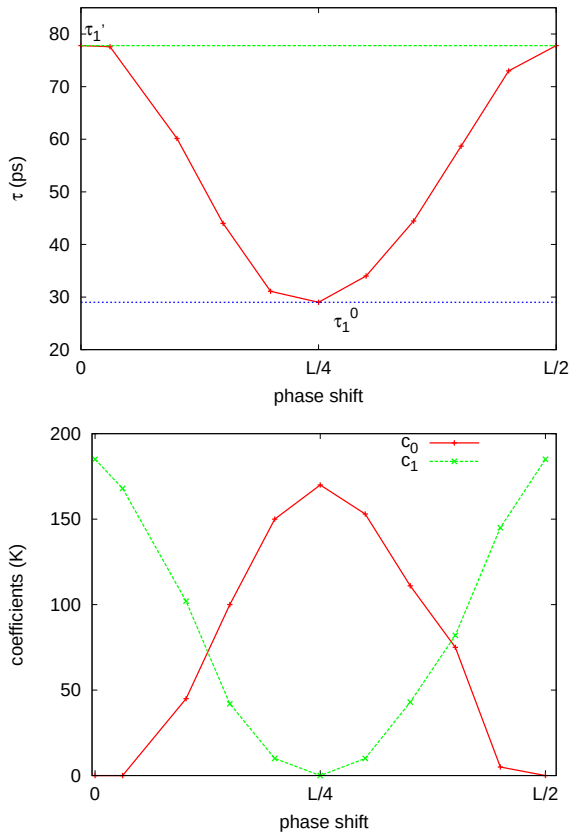

Figure 13: Leading decay time (top panel) and coefficients (bottom panel) in Eq. (47) as function of the phase shift. The data have been obtain by fits of the simulations of a bilayer silicon system of periodicity $L = 250$ nm.

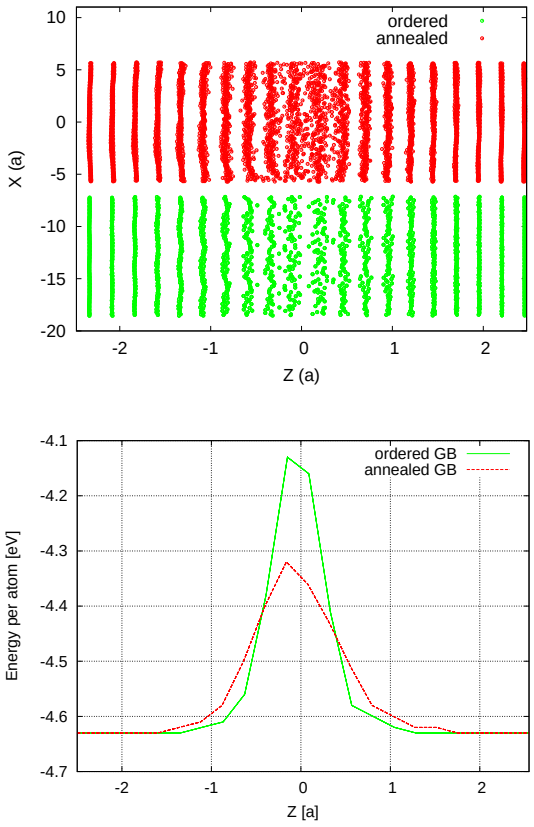

Figure A.14: GB energy profiles and corresponding snapshots of the atomic structure at 0 K. The z-coordinate, normal to the interfaces, is express in units of the lattice parameter.